JGR Oceans

RESEARCH ARTICLE
10.1029/2025JC023433

The Subsurface Symmetric Instability at a Kuroshio Extension Submesoscale Front

Yifan Wang[1,2], **Zhiyou Jing**[1], **Jihai Dong**[3], **Zhaohui Chen**[4,5], **and Haiyuan Yang**[4,5]

[1]State Key Laboratory of Tropical Oceanography, South China Sea Institute of Oceanology, Chinese Academy of Sciences, Guangzhou, China, [2]College of Marine Science, University of Chinese Academy of Sciences, Beijing, China, [3]School of Marine Sciences, Nanjing University of Information Science and Technology, Nanjing, China, [4]Frontier Science Center for Deep Ocean Multi-spheres and Earth System (FDOMES) and Physical Oceanography Laboratory, Ocean University of China, Qingdao, China, [5]Laoshan Laboratory, Qingdao, China

Abstract Submesoscale symmetric instability (SI) is considered to effectively transfer oceanic geostrophic kinetic energy into small-scale dissipation and enhance the vertical exchange of tracers. While SI is widely reported to be active within the ocean boundary layer, only a few studies have claimed the occurrence of SI in the ocean subsurface layer, and the processes that enable subsurface SI development away from the boundary layer still remain poorly understood. Here, based on high-resolution in situ observations in the Kuroshio Extension, the anticyclonic potential vorticity (PV) that favors SI is observed in the subsurface layer (the core is at ∼180 m depth in contrast to the surface mixed layer depth ∼40 m) of an intense submesoscale front with a drastic sea surface temperature change of 12°C across 5 km. The analysis results show that the anticyclonic PV preconditioning subsurface SI is generated at the surface layer due to atmospheric-forced surface buoyancy loss. Subsequently, the diagnosed downward vertical velocity reaches ∼175 m/day, primarily driven by strain-induced frontogenesis and overturning instabilities. These along-isopycnal submesoscale processes facilitate the subduction of surface-origin anticyclonic PV into the subsurface layer. The Lagrangian particle tracking experiments based on model simulation further identify this mechanism. These findings reveal a dynamic pathway linking surface forcing, submesoscale frontogenesis, and the development of subsurface SI, with important implications for the vertical transport of heat, salt, and biogeochemical tracers in frontal regions.

Plain Language Summary Ocean fronts are narrow regions where dense and light waters meet, and they play an important role in controlling the vertical transport of tracers such as heat, salt and carbon in the ocean. One key process at these fronts is symmetric instability (SI), which can drive strong vertical motions along the isopycnals and facilitates mixing. Until now, this process has mainly been observed within the surface and bottom layers, and limited knowledge exists about how it could occur in the ocean interior. Using in situ measurements collected in the Kuroshio Extension, SI was captured below the surface mixed layer. We find that surface cooling makes the upper ocean unstable, and this unstable water is then carried downward along tilted isopycnals by strong frontal flows. This process allows surface water to sink rapidly into deeper layers, at speeds of about 175 m/day. These results reveal that surface forcing can influence the deeper ocean. This mechanism helps move heat, salt, carbon, and other important materials from the surface into the ocean interior.

Key Points:

- Observations reveal subsurface symmetric instability (SI) at a submesoscale front with 12°C sea surface temperature change over 5 km
- Preconditions for subsurface SI arise from negative potential vorticity that is subducted from the surface into the interior on ∼175 m/day
- Subduction processes are primarily driven by strain-induced frontogenesis and along-isopycnal submesoscale instability

Supporting Information:

Supporting Information may be found in the online version of this article.

Correspondence to:

Z. Jing,
jingzhiyou@scsio.ac.cn

Citation:

Wang, Y., Jing, Z., Dong, J., Chen, Z., & Yang, H. (2026). The subsurface symmetric instability at a Kuroshio extension submesoscale front. *Journal of Geophysical Research: Oceans*, *131*, e2025JC023433. https://doi.org/10.1029/2025JC023433

Received 10 SEP 2025
Accepted 10 MAR 2026

Author Contributions:

Data curation: Zhaohui Chen
Supervision: Zhiyou Jing
Writing – original draft: Yifan Wang
Writing – review & editing: Zhiyou Jing, Jihai Dong, Zhaohui Chen, Haiyuan Yang

1. Introduction

Ocean fronts are ubiquitous in the global ocean, as revealed by maps of ocean color, sea surface temperature (SST), or synthetic aperture radar. Particularly, submesoscale fronts, with horizontal scales of ∼10 km and timescales of hours to days, are characterized by Rossby (Ro) and Richardson (Ri) numbers of O(1), indicating the dominance of ageostrophic dynamics and subsequently triggering enhanced vertical velocities larger than those by mesoscale flows (Mahadevan et al., 2008; Siegelman et al., 2020; Tarry et al., 2021). These intense vertical motions, typically on the order of 100 m/day, substantially enhance the vertical exchange of tracers such as heat, salt, nutrients, phytoplankton, and zooplankton larvae between the ocean boundary layer and interior (Lehahn et al., 2007; Lévy et al., 2018; Su et al., 2018; Zhu et al., 2024).

Submesoscale instabilities near the frontal regions also serve as an important physical processes for intensifying oceanic vertical motions. Among these instabilities, symmetric instability (SI) is an important mode and can efficiently extract kinetic energy from the geostrophic flow and trigger a forward energy cascade that leads to energy dissipation and allows ageostrophic overturning motion along slantwise isopycnals (Thomas et al., 2013).

SI mostly occurs when the Ertel potential vorticity (PV; denoted as q) satisfies $fq < 0$, with $q = q_v + q_h$, where the vertical component $q_v = (\zeta + f)\frac{\partial b}{\partial z}$ (b is buoyancy, and ζ is the vertical relative vorticity) satisfies $fq_v > 0$, and the horizontal component $q_h = \left(\frac{\partial u}{\partial z} - \frac{\partial w}{\partial x}\right)\frac{\partial b}{\partial y} + \left(\frac{\partial w}{\partial y} - \frac{\partial v}{\partial z}\right)\frac{\partial b}{\partial x}$ (u and v are horizontal velocities, and w is the vertical velocity) dominates over the q_v (i.e., $|q_h| > |q_v|$). Under this condition, the flow becomes inherently unstable, and this state generally arises only through external forcing, such as frictional and diabatic processes in the boundary layer. Specifically, atmospheric-forced cooling and down-front wind forcing can extract PV and precondition for SI at the surface boundary layer (e.g., Jing et al., 2021; Thomas and Lee, 2005; Thomas & Taylor, 2010). Consistent with this theory, observational studies have documented the occurrence of SI in the ocean surface mixed layer, including aerial observations at the Gulf Stream front (Savelyev et al., 2018) and in situ observations of wind-forced SI at a transient mid-ocean front (Yu et al., 2019). In addition, frictional effects in regions of complex bottom topography, such as ridges, seamounts, and coastal areas, can efficiently extract PV from the bottom boundary layer, further priming the development of SI (Garabato et al., 2019; Gula et al., 2016).

SI has also been documented in the ocean interior, away from both the surface and bottom boundary layers. Observational and modeling studies indicate that SI plays a critical role in the ocean interior by driving turbulent mixing and facilitating energy dissipation. In this study, the ocean interior and subsurface refer to regions below the surface mixed layer. Nagai et al. (2012) used microstructure observations of the Kuroshio front and found that subsurface SI drives intense turbulent mixing, with dissipation rates an order of magnitude higher than wind-driven predictions. Recently, Zhou et al. (2022) provided the first observational evidence of subsurface SI away from surface and topographic boundaries in the equatorial Pacific thermocline, revealing intense turbulent kinetic energy dissipation driven by subsurface SI that can reach nearly 10^{-8} W/kg. In addition, SI enhances the along-isopycnal transport of momentum and tracers, regularly reaching below the mixed layer and enabling vertical exchange between the surface and pycnocline (Freilich & Mahadevan, 2021). Archer et al. (2020) further showed the subsurface SI with slanted overturning cells at the base of the front. This process is likely important for the formation of submesoscale lenses of water beneath the mixed layer. Collectively, these studies highlight that interior SI is a key mechanism for modulating energy dissipation and tracer redistribution, emphasizing its fundamental role in ocean interior dynamics and the vertical transport of heat, salt, and other tracers.

As interior SI plays a critical role in mediating energy dissipation and vertical tracer exchange, it is essential to understand the mechanisms by which SI can develop far from the boundary layer. Since the occurrence of SI requires negative fq, understanding why negative fq is present in the ocean interior is crucial for explaining SI there. According to the impermeability theorem (Haynes & McIntyre, 1987), large volume of negative fq water cannot be directly generated in the ocean interior. This suggests that the ocean interior can only acquire large volume of negative fq from the boundary layer where external forcing extracts PV. One known exception occurs near the equator, where subsurface cross-equatorial currents transport negative PV water from the Southern Hemisphere into the Northern Hemisphere (Zhou et al., 2022). The sign reversal of f across the equator causes fq to become negative once entering the Northern Hemisphere, hence satisfying the necessary condition for SI. Nevertheless, this cross-equatorial mechanism cannot operate in regions far from the equator, where negative fq is widely attributed to frictional and diabatic processes in the boundary layer. In these areas, negative fq is believed to be generated near the surface or topography, and it can be subducted from the surface into the subsurface layer (Archer et al., 2020; Thomas, 2005) or transported along the ridges into the ocean interior (Nagai et al., 2012). Although theoretical studies and limited observations indicate that these pathways may transport boundary-layer negative fq into the ocean interior, more extensive observations are needed to confirm them, particularly regarding subduction from the surface mixed layer into the subsurface layer in the open ocean, away from topographic features.

In the Kuroshio Extension (KE) region, energetic submesoscale fronts exhibit intense vertical motions (Cao et al., 2022; Nagai & Clayton, 2017; Wang et al., 2024; P. R. Yang et al., 2021; Zhu et al., 2024). These strong vertical exchanges are expected to establish dynamic pathways connecting the boundary layer to the ocean interior. Although previous studies have observed subsurface negative fq in the Kuroshio region (Nagai et al., 2012), how SI develops away from the boundary layer, and the associated pathway linking boundary layer and ocean interior, remain poorly understood, as its rapid evolution and small spatial scales make it difficult to capture in observations. In this study, we analyze high-resolution in situ observations collected at a submesoscale front located at the periphery of a mesoscale eddy in the KE region during spring 2016. In addition to the field observations, backward Lagrangian particle tracking based on model simulations is used to further investigate the

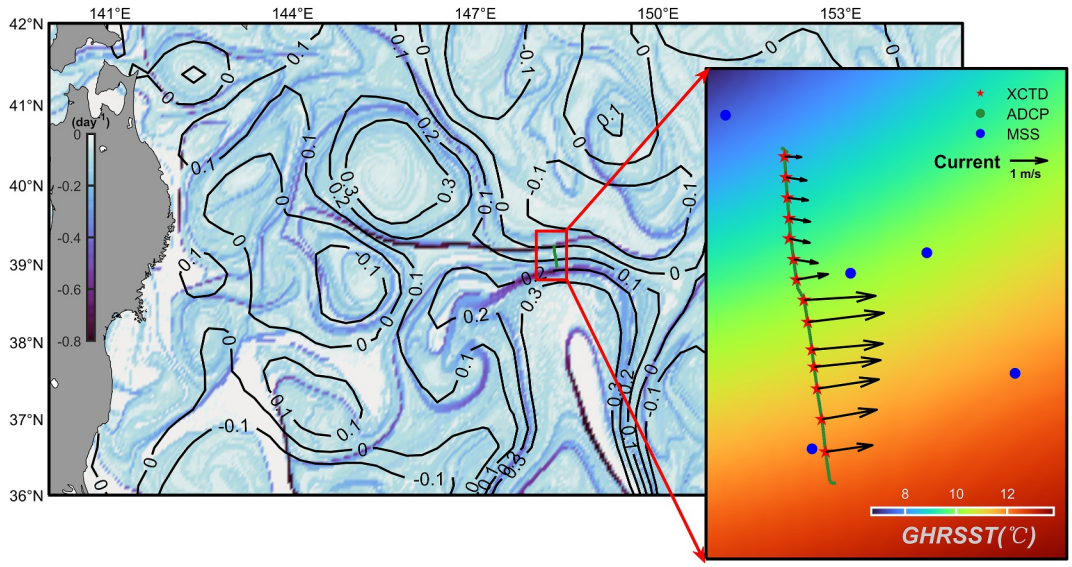

Figure 1. Location of the observation section (green line). The shading color and the black contours show the satellite-observed finite-size Lyapunov exponents and sea level anomaly, respectively. A zooming-in view of the red-box region is shown in the right panel with the sea surface temperature (SST) from the group for high-resolution sea surface temperature. In the panel, the red pentagrams are the expendable conductivity temperature depth locations, while the green and blue dots are the acoustic Doppler current profilers and microstructure system, respectively.

evolution of negative fq water and its pathway into the ocean interior. This study aims to elucidate the underlying generation processes of SI in the ocean interior and to reveal the associated pathway at the submesoscale front. This paper is structured as follows: the in situ observations, other data products, and diagnosed methods used in this study are described in Section 2. Section 3 displays the submesoscale front characteristics and the observed SI in the ocean interior. Section 4 analyzes the evolution of negative fq water and its associated dynamical pathway. Finally, the discussion and summary are in Sections 5.

2. Data and Methods

2.1. In Situ Observations

On 10 April 2016, a targeted observation project focused on a submesoscale front was conducted using the R/V Dongfanghong 2 in the KE region. The transect across the front (from 148.3453°E, 38.9620°N to 148.2904°E, 39.2350°N) is presented in Figure 1 (green dots in the right panel). To capture the characteristics of the rapidly evolving submesoscale front, expendable conductivity temperature depth (XCTD) profilers were deployed at an interval of approximately 2 km within the upper 1,000 m of depth (red pentagrams in Figure 1), with an effective vertical resolution of 1 m. At the same time, the shipboard acoustic Doppler current profilers (ADCP) recorded the horizontal current velocity continuously covering the upper 800-m depth, with a 1-min sampling interval and a 16 m vertical resolution. In addition, the microstructure system (MSS) was deployed to quantify the turbulent shear in the area near the submesoscale front (the blue points in Figure 1).

2.2. Satellite Data and Reanalysis Products

The finite-size Lyapunov exponents (FSLEs) were produced by Archiving, Validation and Interpretation of Satellite Oceanographic data with a spatial resolution of 0.04° (color shading, left panel of Figure 1). The FSLEs are calculated based on geostrophic velocities and provide a method for assessing the velocity at which particles separate in fluid environments. By quantifying particle dispersion or aggregation patterns in the flow, this method reveals the inherent chaotic dynamics and structures, including eddy and frontal regions. The gridded daily sea level anomaly (SLA) data with a spatial resolution of 0.25°, based on satellite altimetry measurements, were obtained from the Copernicus Marine Environment and Monitoring Service (black contours in Figure 1). Sea surface temperature (SST) data (color shading, right panel of Figure 1) were acquired from a multi-sensor and

high-resolution product, the group for high-resolution sea surface temperature (GHRSST), with a spatial resolution of 0.05° and a temporal resolution of 1 day.

In this study, we utilize the fifth generation of the European Center for Medium-Range Weather Forecasts (ECMWF) reanalysis data (ERA5) on single levels to investigate the surface atmospheric forcing conditions over the submesoscale front. We use variables derived from ERA5, including surface downward shortwave and longwave radiation, latent and sensible heat flux, evaporation, precipitation, and sea surface wind. The Global Ocean Physics Reanalysis System product with 1/12° horizontal resolution (GLORYS12V1; Lellouche et al., 2018) was employed to diagnose the surface buoyancy flux along with the front.

2.3. Diagnostic Calculations

2.3.1. Observational Diagnostics

To quantify the submesoscale features of the observed fronts, the normalized vertical relative vorticity (ζ/f) and strain rate (St/f) are calculated based on the observed quantities as

$$\zeta/f = \left(\frac{\partial v}{\partial x} - \frac{\partial u}{\partial y}\right)/f, \tag{1a}$$

and

$$St/f = \sqrt{\left(\frac{\partial u}{\partial x} - \frac{\partial v}{\partial y}\right)^2 + \left(\frac{\partial v}{\partial x} + \frac{\partial u}{\partial y}\right)^2}/f, \tag{1b}$$

where u and v are meridional and zonal velocities in the Cartesian longitude-latitude grids, f is the Coriolis parameter. The in situ transect is oriented nearly meridionally, whereas the front extends primarily in the zonal direction. Therefore, it is assumed that cross-front gradients ($\partial/\partial y$) are much larger than along-front gradients ($\partial/\partial x$). To verify this assumption, the local frontal orientation is estimated from the FSLE gradient field, which indicates that the front deviates by less than 15° from the zonal direction. Thus, the along-front gradient term was neglected (i.e., $\partial/\partial x \approx 0$). By assuming negligible along-front gradients, ζ and St can be simplified as

$$\zeta/f = -(\partial u/\partial y)/f, \tag{2a}$$

and

$$St/f = \sqrt{(\partial u/\partial y)^2 + (\partial v/\partial y)^2}/f. \tag{2b}$$

The investigated Ertel PV (hereafter PV, or represented by the symbol q) can be written as

$$q = (f + \nabla \times u)\cdot\nabla b, \tag{3}$$

where f is the Coriolis parameter, and $u = (u, v, w)$ is the velocity vector. $b = -g\rho/\rho_0$ is the buoyancy, where g is the gravitational acceleration (taken as 9.8 m/s^2 here); ρ and ρ_0 denote the density and the reference density ρ_0 (taken as 1,025 kg/m^3 here). As q can be divided into the vertical component q_v and vertical component q_h, q_v can be calculated by

$$q_v = (f + \zeta)N^2 = (f - \partial u/\partial y)N^2, \tag{4}$$

where $N^2 = \partial b/\partial z$ is the vertical buoyancy gradient. Under conditions of thermal wind balance for the frontal flow (i.e., $\partial u_g/\partial z = -\partial b/\partial y/f$), q_h can be derived as (Thomas, 2008)

$$q_h = -f\left(\frac{\partial u_g}{\partial z}\right)^2 = -\frac{1}{f}\left(\frac{\partial b}{\partial y}\right)^2 = -\frac{M^4}{f}. \tag{5}$$

As the Coriolis parameter f is positive in the Northern Hemisphere and $M^4 > 0$, q_h is a negative definite quantity.

2.3.2. Atmospheric Forcing

To determine the generation mechanism of the observed negative PV at the front, the surface buoyancy forcing processes are investigated. The PV can be modified by surface wind-induced friction over ocean fronts due to the Ekman buoyancy flux (EBF):

$$\mathrm{EBF} = \frac{\tau}{\rho f}\nabla b|_{z=0} \approx -\frac{\tau}{\rho_0 f}\frac{\partial b}{\partial y}|_{z=0}, \tag{6}$$

where τ represents the along-front component of the wind stress, calculated based on the Coupled Ocean-Atmosphere Response Experiment version 3.0 algorithm (COARE 3.0, Fairall et al., 2003). A down-front wind, aligned with the thermal wind shear (i.e., EBF > 0), drives frictional Ekman transport that accumulates dense water above light water. This can sharpen the frontal gradient and weaken vertical stratification, leading to the formation of negative PV. Meanwhile, frontogenesis and instabilities such as SI, gravitational instability (GI), centrifugal instability (CI), and mixed layer instability favor the development of secondary circulation (Dong et al., 2022; Jing et al., 2021), which in turn facilitates the subduction of negative PV into the ocean interior.

The surface buoyancy flux can be written as

$$B_0 = g\alpha_T\frac{Q_{\mathrm{net}}}{\rho_0 C_p} + g\beta(E-P)S_0, \tag{7}$$

where $\alpha_T = 2\times10^{-4}\ ^{\circ}\mathrm{C}^{-1}$ and $\beta = 6\times10^{-4}$ are the thermal expansion and the haline contraction coefficient, respectively, and $C_p = 3850\ \mathrm{J\ kg^{-1}\,^{\circ}C^{-1}}$ denotes the specific heat capacity of seawater. The net air–sea heat flux is $Q_{\mathrm{net}} = Q_{\mathrm{shortwave}} + Q_{\mathrm{longwave}} + Q_{\mathrm{latent}} + Q_{\mathrm{sensible}}$, where the terms represent shortwave radiation ($Q_{\mathrm{shortwave}}$), longwave radiation (Q_{longwave}), latent heat flux (Q_{latent}), and sensible heat flux (Q_{sensible}), respectively. $Q_{\mathrm{shortwave}}$ and Q_{longwave} are sourced from the ERA5, while Q_{latent} and Q_{sensible} are calculated using the COARE 3.0. A negative Q_{net} value indicates the increase of ocean heat and stabilization of the water column, whereas a positive Q_{net} corresponds to heat loss and destabilization. Evaporation (E) and precipitation (P) rates are also derived from the ERA5, and the surface salinity (S_0) is from the GLORYS12V1 reanalysis.

2.3.3. The Generalized Q-Vector Omega-Equation

Based on this observation, the vertical velocity is diagnosed by the generalized Q-vector omega-equation (Giordani et al., 2006):

$$\begin{aligned} f^2\frac{\partial^2 w}{\partial z^2} + \nabla_h\left(N^2\nabla_h w\right) = \nabla_h\cdot\{&\underbrace{-2(\nabla_h u_g)\cdot\nabla_h b}_{Q_{tg}} \underbrace{-2(\nabla_h u_a)\cdot\nabla_h b}_{Q_{\mathrm{tag}}} \underbrace{-f[\nabla_h(k\times u)]\cdot\frac{\partial u_a}{\partial z}}_{Q_{\mathrm{dag}}} \underbrace{-fk\times\frac{D}{Dt}\left(\frac{\partial u_a}{\partial z}\right)}_{Q_{dr}} \\ &\underbrace{-f\frac{\partial}{\partial z}[k\times D_H(u)] - f\frac{\partial}{\partial z}[k\times D_V(u)]}_{Q_{dm}} \underbrace{+\nabla_h[D_H(b)]}_{Q_{\mathrm{rh}}}\}, \end{aligned} \tag{8}$$

where the horizontal velocity u is decomposed into geostrophic and ageostrophic parts ($u = u_g + u_a$), and D_H and D_V represent the horizontal and vertical mixing, respectively. Q_{tg} and Q_{tag} are the kinematic deformations induced by geostrophic and ageostrophic currents. Q_{dag} and Q_{dr} represent the thermal wind imbalance deformation and trend, respectively. Q_{dm} and Q_{rh} are the turbulent forcing of buoyancy and momentum. As described in Qiu et al. (2020), the contributions of Q_{dag} and Q_{dr} are relatively small, so we neglect these two terms in this study. Given that only one transect was available, we apply the two-dimensional simplified version assuming negligible along-front gradients. Thus, the equation along the front can be expressed in a simplified form as

$$f^2\frac{\partial^2 w}{\partial z^2}+\frac{\partial}{\partial y}\left(N^2\frac{\partial w}{\partial y}\right)=-2\frac{\partial}{\partial y}\left(\frac{\partial v}{\partial y}\frac{\partial b}{\partial y}\right)+f\frac{\partial}{\partial y}\frac{\partial^2}{\partial z^2}\left(K_v\frac{\partial u}{\partial z}\right). \quad (9)$$

Here, $K_v = \Gamma\varepsilon/N^2$ denotes the vertical mixing coefficient, where Γ is a constant equal to 0.2 and ε is turbulent kinetic energy dissipation measured from the MSS. Unlike the Quasi-Geostrophic omega-equation, this generalized omega-equation incorporates ageostrophic contributions to the vertical velocity. Considering the small scale of the observed front, the generalized omega-equation enables a more comprehensive assessment of vertical motions in this region. Importantly, surface wind stress is not prescribed directly as a boundary condition. Instead, its effect on vertical velocity is implicitly included through the vertical mixing term K_v.

2.3.4. Instability Criterion

The balanced Richardson number $Ri_B = \left(f^2N^2\right)/|\nabla b|^2$ serves as a diagnostic criterion for identifying the dominant instability types (Thomas et al., 2013), which has been widely used in previous observational studies (e.g., Thompson et al., 2016; Yu et al., 2019; Zheng & Jing, 2024). Following Thomas et al. (2013), we identify instability types by introducing the angle of Ri_B, given by $\phi_{Ri_B} = \tan^{-1}\left(-{Ri_B}^{-1}\right)$ and the critical angle $\phi_C = \tan^{-1}\left(-\frac{\zeta_g}{f}\right)$, where $\zeta_g = f + \nabla \times u_g$. The instability occurs when $\phi_{Ri_B} < \phi_C$. Particularly, the instability criterion for GI, SI, and CI can be identified as the following:

1. GI develops when $N^2 < 0$ and $-180° < \phi_{Ri_B} < -135°$, a hybrid symmetric/gravitational instability (SGI) develops when $-135° < \phi_{Ri_B} < -90°$.
2. For stable stratification ($N^2 > 0$) and cyclonic vertical vorticity, SI develops when $-90° < \phi_{Ri_B} < \phi_C$ with $\phi_C < -45°$. SI is expected to develop when $-90° < \phi_{Ri_B} < -45°$ with $\phi_C > -45°$, for anticyclonic vertical vorticity.
3. CI is expected to develop as $f\zeta_g < 0$ with $N^2 > 0$. And a mixed symmetric/centrifugal instability (SCI) develops when $-45° < \phi_{Ri_B} < \phi_C$ with $\phi_C > -45°$.

2.3.5. Numerical Modeling

To verify the generation and subduction pathway of the negative fq water inferred from the observations, we conducted a set of front-resolving numerical simulations with hydrostatic kernel using the Coastal and Regional Ocean COmmunity (CROCO) model. The model domain spans approximately 110 km across the front and extends vertically to a depth of 1,000 m. To adequately resolve the submesoscale frontal features documented in the observational transects, the model was configured with a uniform horizontal resolution of ~750 m. In the vertical direction, the model uses a terrain-following s-coordinate system with 60 vertical levels. Vertical grid stretching was applied to enhance resolution in the upper ocean and pycnocline region, where sharp density gradients and PV anomalies are concentrated. The stretching parameters were set to $\theta_s = 7$, $\theta_b = 1$, and $hc = 200$ m. Vertical turbulent mixing was parameterized using the K-Profile Parameterization scheme. Momentum advection was computed using the third-order upstream-biased (UP3) scheme. The baroclinic time step was set to 30 s. No explicit lateral Laplacian viscosity or diffusivity was applied.

Initial conditions for temperature, salinity, and along-front velocity were prescribed directly from the observed cross-front hydrographic and velocity section, ensuring consistency between the simulations and observations. Lateral boundary conditions were likewise constrained by the observed section values, providing a dynamically consistent representation of the frontal environment. Surface forcing consisted of an idealized two-phase wind stress sequence, designed to mimic the observed atmospheric forcing during the survey period. Surface heat flux forcing was prescribed with magnitudes and temporal evolution close to the observed conditions, allowing the model to reproduce the observed upper-ocean thermodynamic response while isolating the dynamical processes governing negative PV generation and subduction.

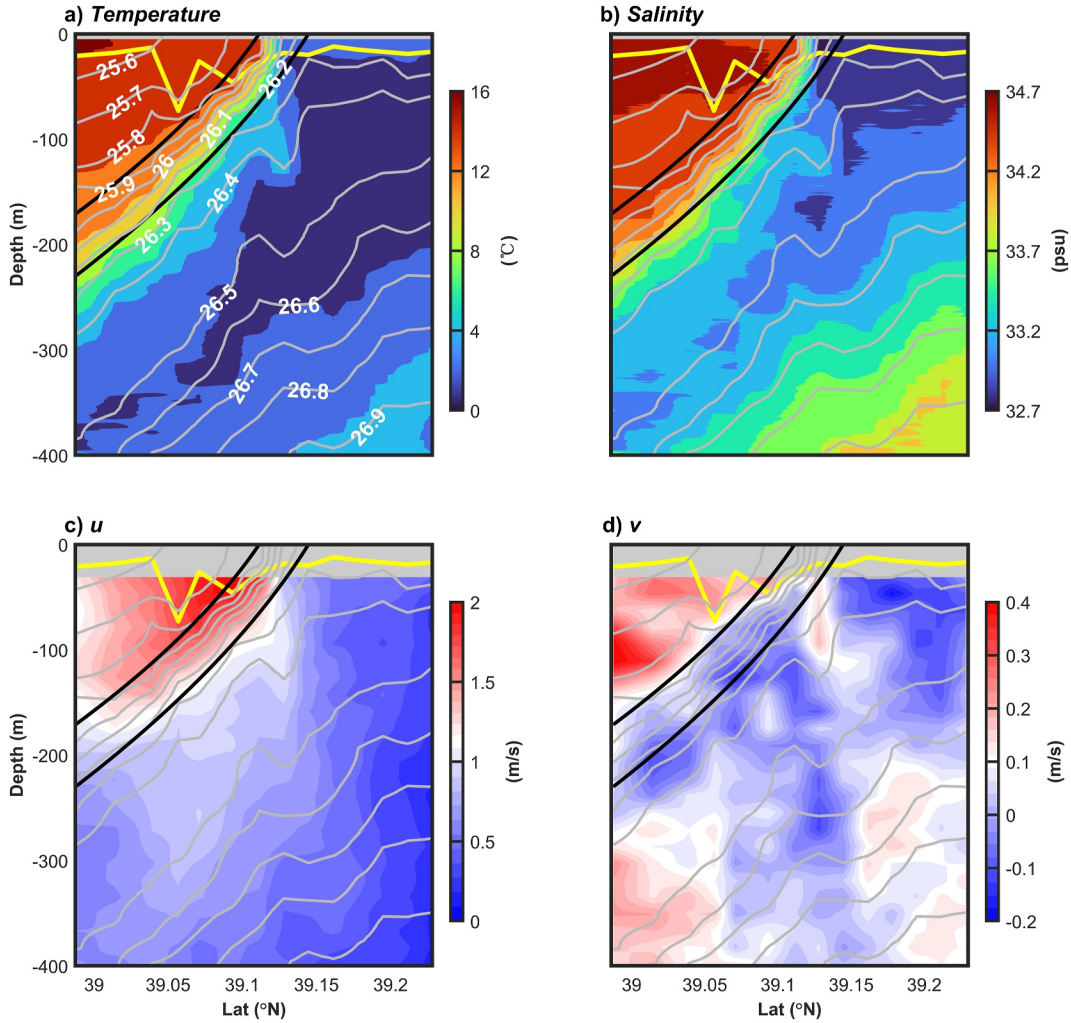

Figure 2. Observed (a) temperature (°C), (b) salinity (psu), (c) u (m/s), and (d) v (m/s) of the submesoscale front. The gray contours represent the isopycnals, with their values labeled in white as −1,000 kg/m^3. The yellow lines represent the mixed layer depth. The black lines mark the frontal region.

3. Observed SI in the Ocean Interior

3.1. Intense Variability Across the Submesoscale Front

According to the vertical profiles from XCTD, a submesoscale front approximately 5 km wide is observed. This front reaches a depth of ∼200 m, while the mixed layer depth is only ∼30 m, defined using a density increase of 0.03 kg m^{-3} relative to 10 m. Significant temperature and salinity variations across the front are shown in Figure 2. In the frontal region, a sharp decrease in SST is observed within the upper 50 m, dropping from 14°C to 2°C over a distance of 5 km (Figure 2a). The corresponding temperature gradient in this area reaches up to approximately 2.4°C/km. One should note that the SST range in Figure 2a is broader than in the GHRSST product (Figure 1). This discrepancy may result from a combination of the nighttime-based observations in Multiscale Ultrahigh Resolution L4 analysis (which miss daytime SST), the spatial smoothing inherent in multi-sensor fusion, and the interpolation of missing data in these areas. The salinity in the upper 50 m layer also presents a sharp gradient of 0.96 psu/km (Figure 2b). This strong gradient is mainly caused by the encounter between the cold and low salinity water mass in the north of the observed site and the warm eddy separated from the KE (Text S1 and Figure S1 in Supporting Information S1). Meanwhile, the along-front velocity (u) at the jet core is 2 m/s in the shallowest layer of the ADCP bin (∼30 m depth), with a 1 m/s change from south to north (Figure 2c). The cross-front velocity (v) is positive at the southern side and negative at the northern side (Figure 2d).

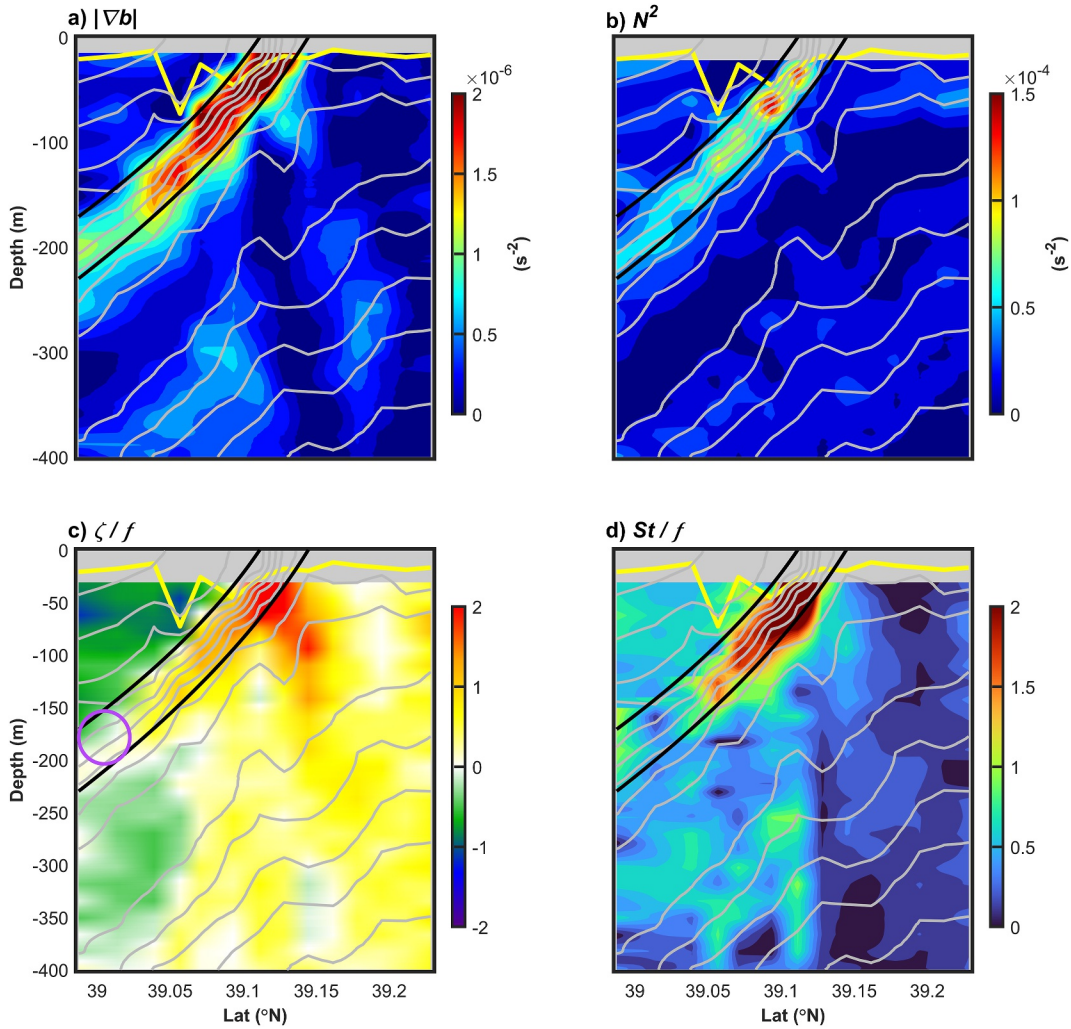

Figure 3. Observed (a) horizontal buoyancy gradient, (b) Brunt-Väisälä frequency N^2, (c) vertical relative vorticity normalized by Coriolis parameter, and (d) strain rate normalized by Coriolis parameter of the submesoscale front. The gray contours are the isopycnals, and the yellow lines represent the mixed layer depth. The black lines mark the frontal region. In panel (c), purple circles highlight the region of anticyclonic vorticity at the base of the front.

Across the submesoscale front, intense temperature and salinity gradients drove a density gradient peaking at 2.2×10^{-4} kg/m^4, corresponding to a buoyancy gradient of 2.15×10^{-6} s^{-2} (Figure 3a). These gradients exhibit the same order as those documented in previous observations of submesoscale fronts in the KE mainstream and Gulf Stream (e.g., D'Asaro et al., 2011; Klymak et al., 2016; Nagai et al., 2012; Whitt et al., 2018; H. Y. Yang et al., 2024). The vertical buoyancy gradient (N^2) is also strong at the frontal region. Although the isopycnals become smoother on the northern side of the section, the temperature there increases with depth. This apparent inconsistency arises because the stratification in this region is primarily controlled by salinity rather than temperature (Text S2 and Figure S2 in Supporting Information S1). In addition, the sharp cross-front velocity variation leads to an O(1) normalized vertical relative vorticity (ζ/f, Figure 3b), indicating a departure from balanced geostrophic motion and subsequently allowing the existence of the ageostrophic dynamics at the front. The SLA and FSLEs reveal that the submesoscale front is located at the periphery of two mesoscale eddies with strong horizontal shear during the period of observation (Figure 1). The strain rate (St) in the region of $\zeta/f \sim$ O(1) is stronger than that in other regions (Figure 3c), indicating the intense lateral stretching at the submesoscale front.

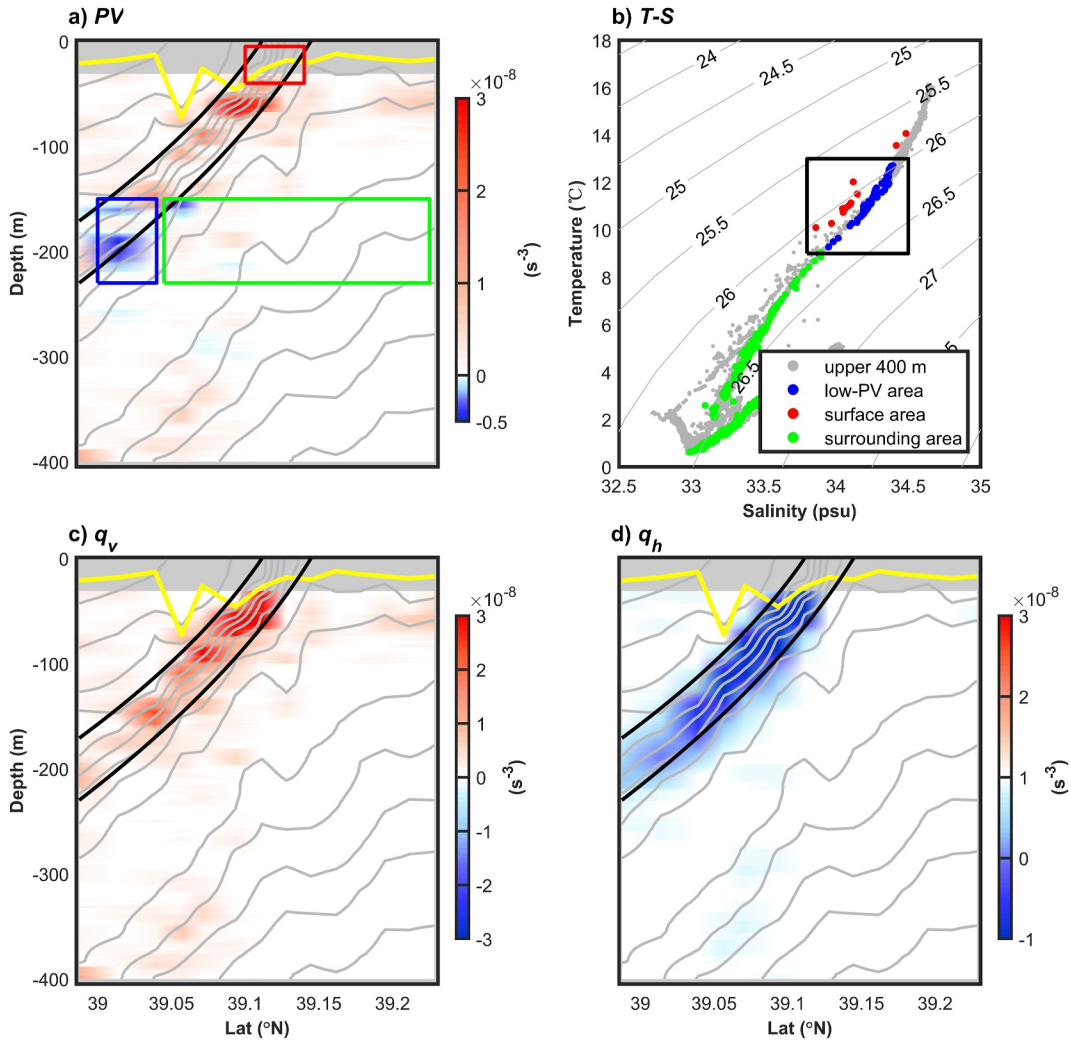

Figure 4. Distribution of (a) total potential vorticity (PV), (b) T–S scatter diagram of the expendable conductivity temperature depth data, (c) the horizontal component of PV (q_h), and (d) the vertical component of PV (q_v). Gray dots in (b) represent data from the upper 400 m, while blue, red, and green dots correspond to data from the regions marked with matching color boxes in (a). The blue box in (a) identifies the region displayed in the zoomed view of Figure 7. The black lines mark the frontal region.

3.2. Structure of Interior SI

The distribution of fq within the submesoscale front, derived from in situ observations, is shown in Figure 4. The fq is basically positive in the upper 150 m (Figure 4a). Both the horizontal (q_h) and vertical (q_v) components of PV exhibit large magnitudes near the front and decay rapidly with depth (Figures 4c and 4d), reflecting the strong vertical shear and buoyancy gradients typical of submesoscale frontal regions. However, a distinct low fq region emerges at approximately 180 m depth near 39.03°N, where the fq approaches zero and even changes sign. This interior negative fq feature is located just beneath the frontal base and is clearly separated from the mixed layer by a band of positive fq (blue box in Figure 4a). Such a vertical structure suggests that different dynamical processes dominate above and below the base of the mixed layer. The low (even negative) fq region coincides with pronounced anticyclonic vorticity and weak stratification (Figures 3b and 3c). The anticyclonic vorticity (marked by purple cycle in Figure 3c) reduces the absolute vorticity $A = \zeta + f$, and together with the weak vertical stratification N^2, results in small values of fq according to Equation 5. This combination of weak N^2 and anticyclonic vorticity has been theoretically associated with conditions favorable for flow instability (Thomas et al., 2013). Thus, the observed negative fq signal in the frontal interior indicates the presence of flow instabilities beneath the surface mixed layer.

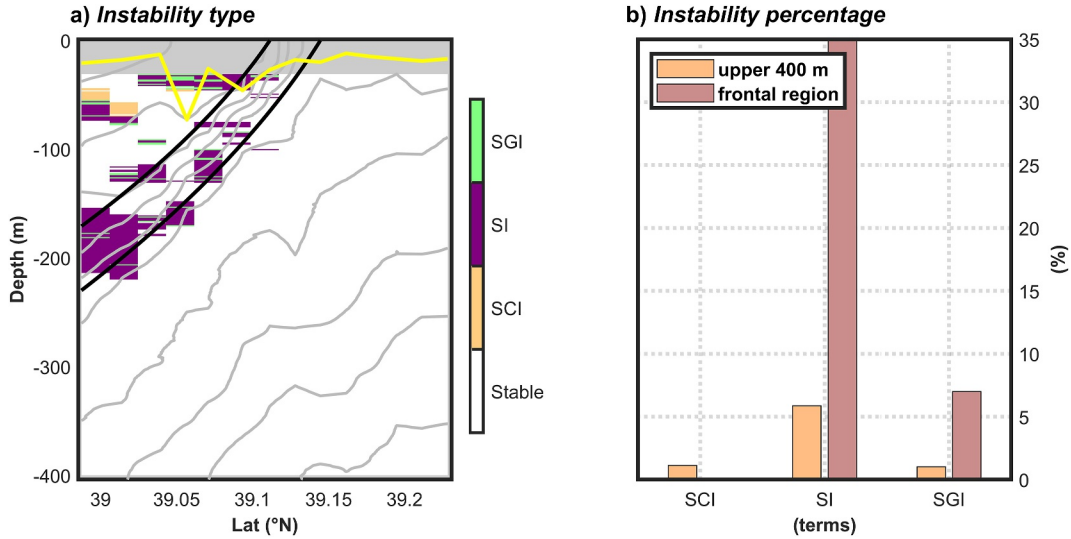

Figure 5. (a) Categorized instability types. (b) The occurrence probability of different instabilities in the upper 400 m (orange) and frontal regions (magenta), respectively. The black lines mark the frontal region.

To assess the instabilities associated with the observed negative fq region, five possible overturning instabilities are diagnosed: GI, CI, SI, SCI, and SGI. Occurrence probabilities of different instabilities are calculated as the fraction of grid points at which each instability type is diagnosed, based on the PV and stratification criteria described in Section 2.3.4. Probabilities are computed separately for all grid points within the frontal region (black lines in Figure 5a) and for the upper 400 m along the transect. The results indicate that SI dominates the overturning processes, with a maximum probability of 33.12% in the frontal region and 5.87% within the upper 400 m. In contrast, the probabilities of GI and CI are approximately 1%, which are not shown here.

The occurrence of negative fq while $N^2 > 0$ and $q_v > 0$ in the frontal interior provides the necessary condition for the development of SI. However, according to the impermeability theorem (Haynes & McIntyre, 1987), large volume of negative fq cannot be generated spontaneously in the open ocean interior. To investigate the origin of the negative fq water mass identified in the frontal interior, we examined the temperature-salinity (T-S) properties from the XCTD profiles within the black-box region highlighted in Figure 4a. The T-S diagram (Figure 4b) reveals that the negative fq water is characterized by an average temperature of 11°C and salinity of 34.3 psu, closely matching the properties of the surface mixed layer water at the frontal region (red dots in Figure 4b). In contrast, the water mass outside the frontal region at the same depth exhibits markedly different T-S characteristics (green dots), indicating that the interior $fq < 0$ water is not entrained from the surrounding thermocline but is dynamically linked to the frontal surface layer.

4. Generation and Subduction of Negative fq

As we have identified that the negative fq needed to drive SI originates from the surface, the processes responsible for its generation and the pathways through which it is transported into the ocean interior remain unclear. This motivates a detailed investigation of the source and transport pathways of negative fq in the frontal region, aiming to clarify the processes that drive surface negative fq water into the ocean interior. In the following section, we analyze the generation of negative fq based on in situ and reanalysis data, infer the direction of its transport from diagnosed vertical velocities, and further verify its transport pathways using a three-dimensional process study model combined with the backward Lagrangian particle tracking method.

4.1. Generation of Negative fq

The surface PV can be modified using frictional and diabatic processes at isopycnal outcrops (Thomas, 2005). These processes locally redistribute momentum and buoyancy, and are inherently transient, as they can trigger SI and lead to mixing, ultimately restoring the flow toward a stable configuration. To investigate how observed negative fq water is generated at the submesoscale front, the atmospheric conditions above the front are examined

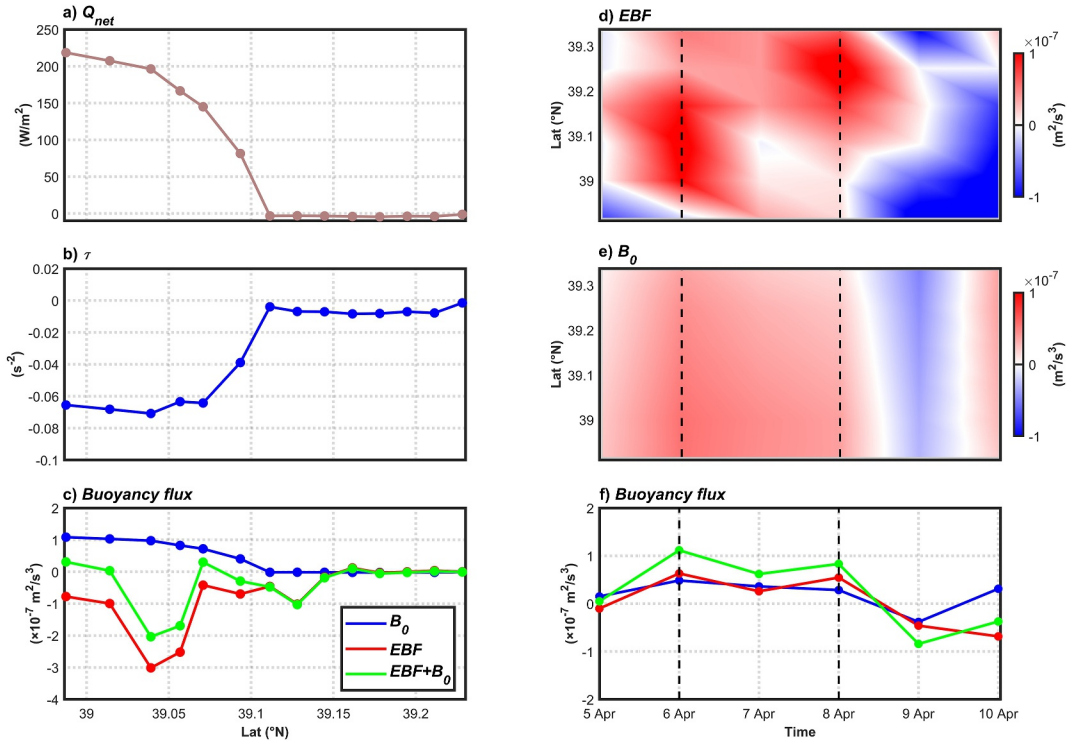

Figure 6. Atmospheric forcing during in situ sampling: (a) the total heat flux Q_{net} (positive values indicate ocean heat loss), (b) wind stress; (c) the surface buoyancy flux along the transect induced by B_0 (blue line) and EBF (red line). The time–latitude Hovmöllers of (d) EBF and (e) B_0 are calculated from ERA5 and GLORYS12 data, and their contribution to buoyancy flux is plotted in (f).

during this period (Figure 6). The calculated air-sea heat flux show a heat loss reaching 220 W/m^2 from the sea surface into the atmosphere over the frontal region (Figure 6a), which destabilizes the sea water instability. The heat fluxes contribute to the surface buoyancy loss with an average magnitude of 3.5×10^{-8} m^2/s^3 in the frontal region and can subsequently lead to $fq < 0$ (Haine & Marshall, 1998), potentially intensifying the frontogenesis and further enhancing subduction (Yoshikawa et al., 2001). While the front undergoes a cooling effect, the wind-induced surface buoyancy fluxes exhibit greater fluctuations (Figures 6b and 6c). The wind stress displayed a significant change, with its magnitude varying by 0.06 m/s^2 across the front within 5 km. During in situ sampling, the up-front wind produced an average negative EBF of -7.1×10^{-8} m^2/s^3 within the frontal region. Consequently, the greater stabilizing effect of wind forcing counterbalance instability in the water column generated by surface heat flux during the sampling period.

However, the surface buoyancy loss is influenced by both down-front wind and surface cooling before in situ sampling period (6th–8th April; Figures 6d–6f). Due to limited observational data, we hypothesize that this wind forcing produced the negative fq observed on April 10, likely persisting as a remnant from a larger negative fq area to later mixing and dissipation. Previous studies have shown that within the surface mixed layer, negative fq tend to be removed following down-front wind relaxation. For example, Mahadevan (2016) has noted that it may require several inertial periods to mix out negative fq, while Taylor and Ferrari (2009) proposed a persistent "fossil remnant mode" of SI characterized by a longer wavelength, which follows the most unstable mode and acts to return the negative fq to zero in the surface mixed layer. In contrast, below the surface mixed layer, Archer et al. (2020) found that subsurface negative fq can persist for more than two inertial periods. Consistent with this subsurface persistence, our observations show that negative fq emerges at the base of the front, distant from the area where stabilizing wind exerts its influence. This observed negative fq was captured within approximately 36 hr after the down-front wind relaxation (Figure 6f), not exceeding two inertial periods (19 hr at 39°N).

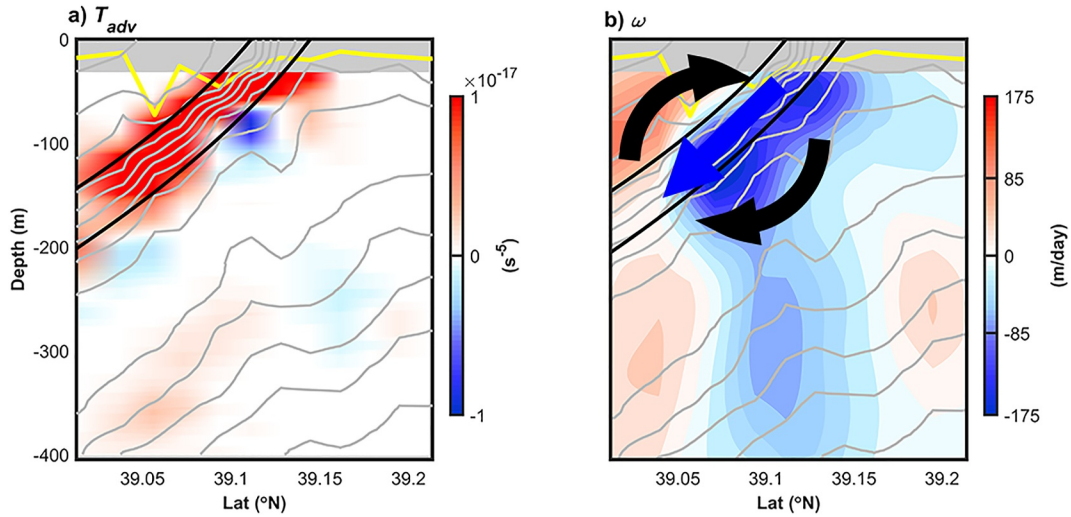

Figure 7. The inferred cross-front secondary circulation. (a) The horizontal advection term of frontogenetic tendency. (b) Vertical velocity, with black arrows indicating the frontal circulation and blue arrow indicating subduction along the front. The gray yellow lines represent the isopycnals and the mixed layer depth, respectively. The black lines denote the frontal region.

4.2. Subduction and Isolation

Following the formation of negative fq at the surface through atmospheric forcing, we next investigate how this surface-origin water is transported into the ocean interior. The subduction of negative fq water is closely linked to the frontal secondary circulation, which arises from the sloping isopycnals and cross-front density gradients associated with the submesoscale front. At the submesoscale front, the frontal secondary circulation can be enhanced during frontogenesis. The horizontal advection term of frontogenesis tendency can be calculated by $T_{\mathrm{adv}} = -(\frac{\partial v}{\partial y}\frac{\partial b}{\partial y})\frac{\partial b}{\partial y}$. As shown in Figure 7a, T_{adv} is mainly positive along the frontal region. This indicates that the horizontal straining effect tends to sharpen the front, implying a strong frontal second circulation arise.

The cross-front secondary circulation can be estimated using the generalized Q-vector omega-equation, based on the observed sloping frontal stratification and cross-front convergence. The diagnosed vertical velocity (w) field is calculated by solving the two-dimensional generalized Q-vector omega-equation using the observed temperature, salinity, turbulent kinetic energy dissipation rate (ε), and horizontal velocity. One should note that the two-dimensional Q-vector generalized omega equation used here is subject to certain limitations, as the along-front variations were neglected. Nevertheless, the contribution of along-front gradients is expected to be much smaller than that of cross-front variations in this case. Consistent with the theoretical prediction, w is downward (upward) velocity on the heavy (light) side of the front, with a vertical structure penetrating to 200 m depth. This implies that the secondary circulation tends to facilitate dense front subduction. The diagnosed vertical velocities reached approximately 175 m/day in the frontal region (Figure 7b). These intense vertical motions not only drive the subduction but also enhance the vertical exchange of heat, salt, and other tracers between the upper layer and the ocean interior.

The strong downward motions diagnosed in the secondary circulation provide a pathway for surface-origin negative fq water to subduct into the ocean interior. Focusing on the region highlighted by the black box in Figure 4a, we examine the PV distribution to quantify the vertical and horizontal contributions to the PV budget and to identify the dominant processes controlling the subduction. In this zone, the vertical component of PV is relatively small due to stable but weak stratification, while the strong horizontal shear enhances the baroclinic component. According to our calculations, the cross-section through the negative fq region shows that q_h is approximately -3×10^{-9} s^{-3} and q_v is around zero (Figures 8a and 8d). This suggests that q_h plays the dominant role in generating negative fq, and further resulting in SI.

To clarify the mechanism responsible for the negative fq at the base of the front, the PV budget equation is derived as

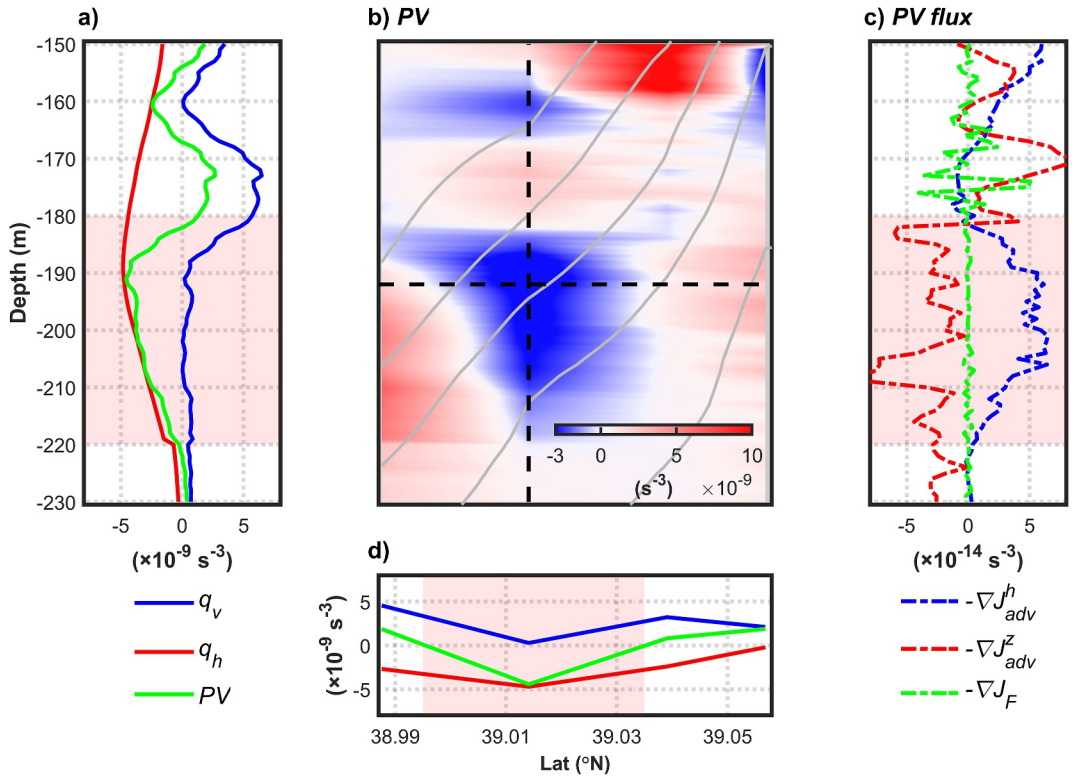

Figure 8. Zoomed-in view of the black box in Figure 4a for (a) the vertical profiles of potential vorticity (PV) terms, (b) the distribution of PV, (c) the vertical variation of PV flux, and (d) the meridional variation of PV flux. Ertel PV (green line), q_v (blue line), and q_h (red line) in (a) and (d) are correspond to the vertical and horizontal dashed black line in (b), respectively. (c) shows the PV flux terms along the vertical black dashed line in (b), where the blue dashed line represents the horizontal advection term, the red dashed line represents the vertical advection, and the green dashed line represents the PV flux induced by friction.

$$\frac{\partial q}{\partial t} = -\nabla J, \tag{10}$$

where J is the J-flux term, consisting of the advection, friction, and non-adiabatic terms, that is,

$$J = uq - F \times \nabla b - (fk + \omega) D. \tag{11}$$

Here, uq represents the advection of PV by background currents; $F = \frac{\partial}{\partial z}\left(K_v \frac{\partial u}{\partial z}\right)$ is the vertical turbulence friction force; $(fk + \omega)$ is the total vorticity; $D = \frac{db}{dt}$ denotes the diabatic buoyancy term; and hence $(fk + \omega) D$ is related to the non-adiabatic effect. The terms of advection $(-\nabla J_{\text{adv}} = -\nabla uq)$ and friction $(-\nabla J_F = \frac{\partial}{\partial z}\left(\frac{\partial}{\partial z}\left(K_v \frac{\partial u}{\partial z}\right) \cdot \frac{\partial b}{\partial y}\right) - \frac{\partial}{\partial y}\left(\frac{\partial}{\partial z}\left(K_v \frac{\partial u}{\partial z}\right) \cdot \frac{\partial b}{\partial z}\right))$ are calculated in this study. The advection term is derived into horizontal $(-\nabla J^h_{\text{adv}} = -\frac{\partial}{\partial y}(vq))$ and vertical parts $(-\nabla J^z_{\text{adv}} = -\frac{\partial}{\partial z}(wq))$.

As shown in Figure 8c, both the horizontal and vertical advective processes dominate the PV budget, while the mixing is weak in the ocean interior. The horizontal component $-\nabla J^h_{\text{adv}}$ is primarily positive within the range of 150–230 m, indicating an increase in PV, while the vertical component $-\nabla J^z_{\text{adv}}$ is negative between 180 and 220 m, suggesting a decrease in PV. Consequently, the subduction of negative fq water is dominated by vertical convection. This result of in situ observation is consistent with the previous numerical simulation and theoretical prediction results (e.g., Thomas, 2008; Thomas & Lee, 2005): the intense downward vertical motions can rapidly subduct the negative fq water from surface into ocean interior. Then the negative fq provides the favorable conditions for the development of SI in the ocean interior.

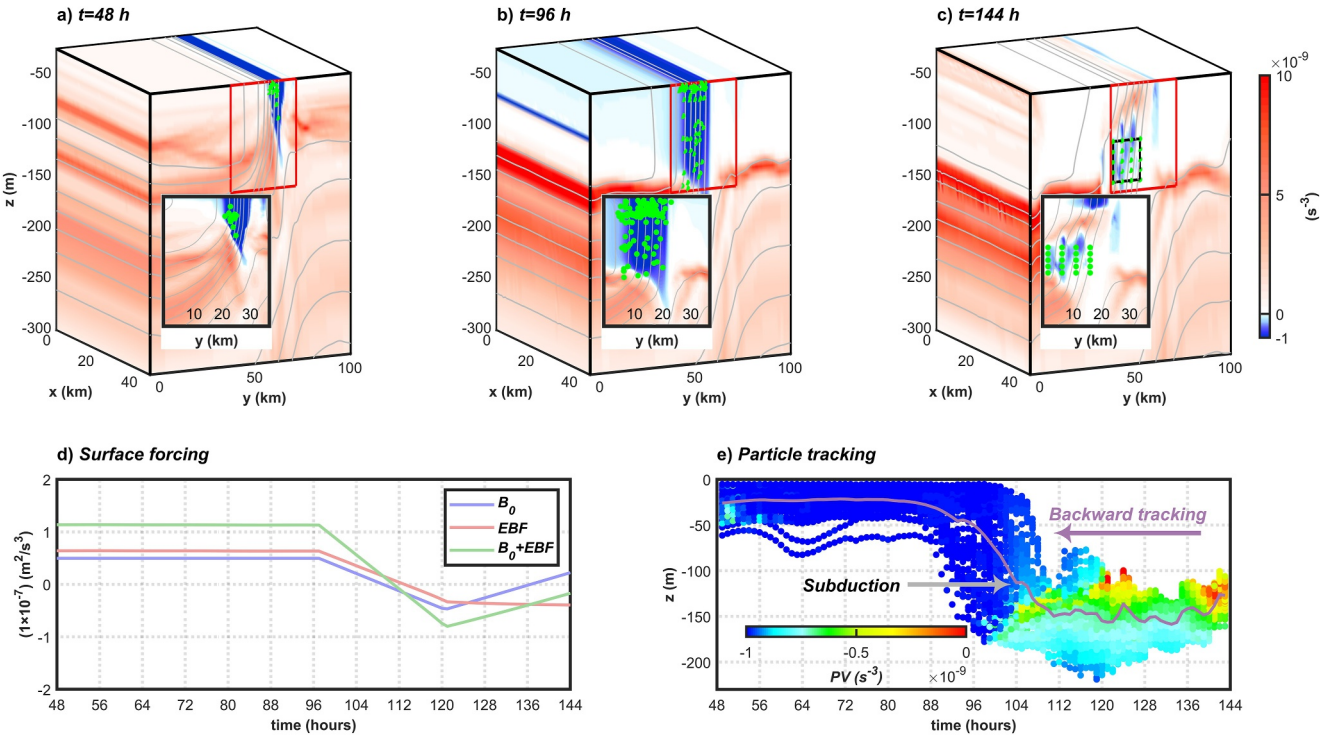

Figure 9. Evolution of potential vorticity (PV) and surface forcing. (a–c) The PV at 48, 96, and 144 hr. Red boxes in (a–c) indicate regions shown in the corresponding zoomed-in insets. (d) Surface buoyancy flux, with positive (negative) values indicating buoyancy gain (loss). (e) Backward particle trajectories from the 144 hr negative fq core (black box in c), with color shading indicating particle PV values. The green dots in (a–c) reveal the particle locations.

4.3. Subduction Process Simulations

A process study model CROCO is used to examine the generation and subduction pathway of the negative fq water inferred from the observations. The model reproduces the observed front under varying atmospheric forcing, enabling us to analyze the dynamical response of the mixed layer to surface buoyancy gain and loss conditions (Figure 9d). The evolution of PV at 48, 96, and 144 hr is shown in Figures 9a–9c. During the surface buoyancy loss stage (48 hr), negative fq rapidly develops near the surface, indicating the onset of strong frontal instability. As the forcing persists, the $fq < 0$ region extends downward along sloping isopycnals, reaching depths of approximately 200 m after 48 hr. When the atmosphere transitions to a buoyancy-gaining phase (112–144 hr), positive PV begins to be injected into the ocean, and the previously formed negative fq layer becomes progressively separated from the surface by a newly developed positive fq cap. This process results in a subsurface negative fq remnant trapped at the base of the front. The subsurface negative fq extends roughly 10 km across the front, consistent with the frontal width. The temporal evolution of surface buoyancy flux (Figure 9d) provides a consistent dynamic interpretation of this transition. Between 48 and 112 hr, the surface buoyancy flux remains positive ($B_0 + \mathrm{EBF} > 0$), indicating buoyancy loss from the ocean and the removal of PV from the surface layer, which favors the generation and deepening of negative fq water. From 112 to 144 hr, however, $B_0 + \mathrm{EBF}$ becomes negative ($B_0 + \mathrm{EBF} < 0$), signifying that the atmosphere injects PV into the ocean. This stabilizing regime results in the development of a surface positive fq cap that isolates the subducted negative fq water beneath it.

To further clarify the origin and evolution of the subsurface negative fq anomaly, we performed backward Lagrangian particle tracking using velocity fields from the model. Specifically, a total of 25,700 passive particles were released at the core of negative fq (black box in Figure 9c) from the 144 hr and advected backward in time for 96 hr (Figure 9e). The trajectories were computed from the model's hourly averaged three-dimensional velocity fields using a fourth-order Runge–Kutta integration scheme. The results clearly show that most particles originate from the surface mixed layer during the buoyancy-loss stage and subsequently descend along tilted

isopycnals into the ocean interior, closely following the frontal sloping structure. Spatially, the trajectories are strongly confined within the frontal zone, further emphasizing that the submesoscale frontal circulation predominantly governs the transport pathway (Figures 9a–9c). Notably, the PV values carried by these particles are large near the surface and progressively increase during descent, while remaining negative throughout the subduction process. This reflects not only the weakening influence of surface friction and diabatic forcing with depth, but also the effect of negative fq-induced instabilities, which generate secondary circulations that restratify the ocean, enhance stratification, and reduce lateral buoyancy gradients, thereby stabilizing the flow. This gradual evolution further confirms that the observed subsurface fq anomaly originates from the surface and is subducted into subsurface along sloping isopycnals. Collectively, the particle-tracking results, together with the process model diagnostics, consistently delineate a dynamical pathway linking atmospheric forcing, frontogenesis, and ocean interior SI.

5. Discussion and Conclusion

A drastic submesoscale front characterized by Rossby numbers (Ro) of O(1) is observed in the KE region. In this front, significant changes occur across the front within the upper 50 m: the temperature drops from 14°C to 2°C and salinity from 34.7 psu to 32.7 psu over a distance of 5 km. The intense cross-frontal changes in temperature and salinity sharpen the density gradient, driving peak values of 2.4×10^{-4} kg/m^4, corresponding to a buoyancy gradient of 2.15×10^{-6} s^{-2} (Figure 3a). Meanwhile, the along-front velocity u at the jet core reaches 2 m/s with a 1 m/s change across the front. The sharp cross-front velocity variation leads to the normalized vertical relative vorticity ζ/f of O(1) that indicates a departure from balanced geostrophic motion. A strain magnitude of $\zeta/f \sim$ O(1) signifies the intense lateral straining at the submesoscale front.

During the in situ observation, a distinct negative fq was detected at ∼180 m depth, associated with anticyclonic vorticity and weak stratification. The thermohaline properties of this water mass match those of surface mixed-layer waters, confirming its surface origin. The overlying positive fq isolates the negative fq core from the surface, suggesting a subsurface remnant that preserves the signature of surface processes. Importantly, diagnostics indicate that the local PV satisfy the criteria for SI, suggesting active SI within the subsurface layer. However, the occurrence of SI at this depth is inconsistent with classical theory, which predicts that SI primarily develops in the surface mixed layer or near strong boundary forcing. A process study model and backward Lagrangian particle tracking further confirm that this negative fq water is transported from the surface mixed layer along tilted isopycnals into the ocean interior. The generation of negative fq and the onset of SI are closely linked to mesoscale strain-induced frontogenesis and surface-forced buoyancy loss. Frontogenesis strengthens lateral buoyancy gradients, enhancing q_h and preconditioning the flow for SI. The subsequent slantwise convection associated with SI drives vigorous secondary circulations with vertical velocities of O(100 m day^{-1}), facilitating the rapid downward transport of surface waters along the frontal isopycnals.

However, other mechanisms may also contribute to the enhanced vertical velocities observed in this study. Internal waves, including near-inertial waves and high-frequency internal tides, can generate substantial vertical motions (Cao et al., 2022). In addition, the vertical transport associated with mixed layer instability can extend below the mixed layer, inducing significant vertical motions. Zhang (2024) proposed that this mechanism could enhance subsurface vertical exchange, modulated by frontogenesis. Although we did not consider the dynamics of internal waves or this instability in this study, it is possible that both could play an important role in the observed vertical velocities. Future studies, using higher-frequency observations and high-resolution simulations, will be essential to disentangle the contributions of SI and internal waves, and to better quantify their combined impacts on vertical transport and tracer exchange in frontal regions.

In summary, our results indicate that submesoscale fronts provide an efficient pathway by which surface waters carrying negative fq are transported into the ocean interior, where they can develop SI under preconditioned weak stratification. The frontogenestic vertical secondary circulation facilitates the downward transport of negative fq water, promoting rapid subduction of heat, salt, carbon, and dissolved gases from the surface into the interior. By combining high-resolution observations, PV diagnostics, and front-resolving model simulations, this study links atmospheric forcing, submesoscale front, and surface-origin negative fq water to the formation of subsurface SI and its subsequent pathway into the ocean interior. These findings highlight the critical role of submesoscale instabilities in mediating thermocline ventilation, reveal the pathway connecting the boundary layer to deeper

layers, and suggest that similar mechanisms may operate in other regions with energetic submesoscale fronts, carrying broad implications for ocean mixing and the transport of climate-relevant tracers (Lévy et al., 2018; Li & Gan, 2025; Omand et al., 2015; Qu et al., 2022).

Conflict of Interest

The authors declare no conflicts of interest relevant to this study.

Availability Statement

The submesoscale front observational data utilized in this study are available at https://zenodo.org/records/10428582 (H. Yang & Chen, 2023). The FSLEs data is available at https://doi.org/10.24400/527896/a01-2022.002 (Archiving, Validation, and, Interpretation of Satellite Oceanographic Data, 2021). The sea level anomaly product is obtained from https://doi.org/10.48670/moi-00145 (Sea Level Anomaly, 2023). The GHRSST data is accessible at https://podaac.jpl.nasa.gov/dataset/MUR-JPL-L4-GLOB-v4.1 (GHRSST, 2015). The ERA5 products are from the ECMWF (Hersbach et al., 2023). The version of the COARE 3.0 algorithm is available at https://github.com/NOAA-PSL/COARE-algorithm/tree/5b144cf6376a98b42200196d57ae40d791494abe/Matlab/COARE3.0 (COARE3.0, 2013). The source code of the CROCO model is obtained from https://zenodo.org/records/17208523 (Auclair et al., 2025). The model output and the scripts used to generate the figures have now been made publicly available at https://github.com/Kris19999/For-JGRO-The-Subsurface-Symmetric-Instability-at-a-Kuroshio-Extension-Submesoscale-Front-.git.

Acknowledgments
This research is supported by the National Natural Science Foundation of China (42225602, 42530403), the National Key Research and Development Program of China (2023YFC3008003), and partly by the National Natural Science Foundation of China (42176023, 42225601, 42422601, 42149907, 42349584, 42349907, 42549907). The authors extend their gratitude to the crew of the R/V Dongfanghong 2 for all the support during the cruise.

References

Archer, M., Schaeffer, A., Keating, S., Roughan, M., Holmes, R., & Siegelman, L. (2020). Observations of submesoscale variability and frontal subduction within the mesoscale eddy field of the Tasman Sea. *Journal of Physical Oceanography*, *50*(5), 1509–1529. https://doi.org/10.1175/JPO-D-19-0131.1

Archiving, Validation, and, Interpretation of Satellite Oceanographic Data. (2021). Finite-size Lyapunov exponents and orientations of the associated eigenvectors [Dataset]. *AVISO*. https://doi.org/10.24400/527896/a01-2022.002

Auclair, F., Benshila, R., Bordois, L., Boutet, M., Brémond, M., Caillaud, M., et al. (2025). Coastal and regional ocean COmmunity model (2.1.1) [Software]. *Zenodo*. https://doi.org/10.5281/zenodo.17208523

Cao, H. J., & Jing, Z. Y. (2022). Submesoscale ageostrophic motions within and below the mixed layer of the Northwestern Pacific Ocean. *Journal of Geophysical Research: Oceans*, *127*, e2021JC017812. https://doi.org/10.1029/2021JC017812

COARE3.0. (2013). GitHub [Software]. Retrieved from https://github.com/NOAA-PSL/COARE-algorithm/tree/5b144cf6376a98b42200196d57ae40d791494abe/Matlab/COARE3.0

D'Asaro, E., Lee, C., Rainville, L., Harcourt, R., & Thomas, L. (2011). Enhanced turbulence and energy dissipation at Ocean fronts. *Science*, *332*(6027), 318–322. https://doi.org/10.1126/science.1201515

Dong, J. H., Jing, Z. Y., Fox-Kemper, B., Wang, Y. T., Cao, H. J., & Dong, C. M. (2022). Effects of symmetric instability in the Kuroshio extension region in winter. *Deep-Sea Research Part II*, *202*, 105142. https://doi.org/10.1016/j.dsr2.2022.105142

Fairall, C. W., Bradley, E. F., Hare, J. E., Grachev, A. A., & Edson, J. B. (2003). Bulk parameterization of air-sea fluxes: Updates and verification for the COARE algorithm. *Journal of Climate*, *16*(4), 571–591. https://doi.org/10.1175/1520-0442(2003)016<0571:bpoasf>2.0.co;2

Freilich, M., & Mahadevan, A. (2021). Coherent pathways for subduction from the surface mixed layer at Ocean fronts. *Journal of Geophysical Research: Oceans*, *126*(5), e2020JC017042. https://doi.org/10.1029/2020JC017042

Garabato, A. C. N., Frajka-Williams, E. E., Spingys, C. P., Legg, S., Polzin, K. L., Forryan, A., et al. (2019). Rapid mixing and exchange of deep-ocean waters in an abyssal boundary current. *Proceedings of the National Academy of Sciences of the United States of America*, *116*(27), 13233–13238. https://doi.org/10.1073/pnas.1904087116

GHRSST. (2015). JPL MUR MEaSUREs project [Dataset]. *GHRSST Level 4 MUR Global Foundation Sea Surface Temperature Analysis (v4.1)*. https://doi.org/10.5067/GHGMR-4FJ04

Giordani, H., Prieur, L., & Caniaux, G. (2006). Advanced insights into sources of vertical velocity in the ocean. *Ocean Dynamics*, *56*(5–6), 513–524. https://doi.org/10.1007/s10236-005-0050-1

Gula, J., Molemaker, M. J., & McWilliams, J. C. (2016). Topographic generation of submesoscale centrifugal instability and energy dissipation. *Nature Communications*, *7*(1), 12811. https://doi.org/10.1038/ncomms12811

Haine, T. W. N., & Marshall, J. (1998). Gravitational, symmetric, and baroclinic instability of the ocean mixed layer. *Journal of Physical Oceanography*, *28*(4), 634–658. https://doi.org/10.1175/1520-0485(1998)028<0634:GSABIO>2.0.CO;2

Haynes, P. H., & McIntyre, M. E. (1987). On the evolution ofvorticity and potential vorticity in the presence of diabatic heating and friction or other forces. *Journal of the Atmospheric Sciences*, *44*(5), 828–841. https://doi.org/10.1175/1520-0469(1987)044<0828:OTEOVA>2.0.CO;2

Hersbach, H., Bell, B., Berrisford, P., Biavati, G., Horányi, A., Muñoz Sabater, J., et al. (2023). ERA5 hourly data on pressure levels from 1940 to present [Dataset]. *Copernicus Climate Change Service (C3S) Climate Data Store (CDS)*. https://doi.org/10.24381/cds.bd0915c6

Jing, Z. Y., Fox-Kemper, B., Cao, H. J., Zheng, R. X., & Du, Y. (2021). Submesoscale fronts and their dynamical processes associated with symmetric instability in the Northwest Pacific subtropical Ocean. *Journal of Physical Oceanography*, *51*(1), 83–100. https://doi.org/10.1175/Jpo-D-20-0076.1

Klymak, J. M., Shearman, R. K., Gula, J., Lee, C. M., D'Asaro, E. A., Thomas, L. N., et al. (2016). Submesoscale streamers exchange water on the north wall of the Gulf Stream. *Geophysical Research Letters*, *43*(3), 1226–1233. https://doi.org/10.1002/2015GL067152

Lehahn, Y., d'Ovidio, F., Lévy, M., & Heifetz, E. (2007). Stirring of the northeast Atlantic spring bloom: A Lagrangian analysis based on multisatellite data. *Journal of Geophysical Research*, *112*, C08005. https://doi.org/10.1029/2006jc003927

Lellouche, J. M., Greiner, E., Le Galloudec, O., Garric, G., Regnier, C., Drevillon, M., et al. (2018). Recent updates to the copernicus marine service global ocean monitoring and forecasting real-time 1/12° high-resolution system. *Ocean Science*, *14*(5), 1093–1126. https://doi.org/10.5194/os-14-1093-2018

Lévy, M., Franks, P. J. S., & Smith, K. S. (2018). The role of submesoscale currents in structuring marine ecosystems. *Nature Communications*, *9*(1), 4758. https://doi.org/10.1038/s41467-018-07059-3

Li, X. Y., & Gan, B. L. (2025). Modulation of Oceanic CO2 uptake by the Kuroshio extension bimodal States. *Geophysical Research Letter*, *52*(12), e2025GL116195. https://doi.org/10.1029/2025GL116195

Mahadevan, A. (2016). The impact of submesoscale physics on primary productivity of Plankton. *Annual Review of Marine Science*, *8*(1), 161–184. https://doi.org/10.1146/annurev-marine-010814-015912

Mahadevan, A., Thomas, L. N., & Tandon, A. (2008). Comment on eddy/wind interactions stimulate extraordinary mid-ocean plankton blooms. *Science*, *320*(5875), 448. https://doi.org/10.1126/science.1152111

Nagai, T., & Clayton, S. (2017). Nutrient interleaving below the mixed layer of the Kuroshio extension front. *Ocean Dynamics*, *67*(8), 1027–1046. https://doi.org/10.1007/s10236-017-1070-3

Nagai, T., Tandon, A., Yamazaki, H., Doubell, M. J., & Gallager, S. (2012). Direct observations of microscale turbulence and thermohaline structure in the Kuroshio front. *Journal of Geophysical Research*, *117*(C8). https://doi.org/10.1029/2011jc007228

Omand, M. M., D'Asaro, E. A., Lee, C. M., Perry, M. J., Briggs, N., Cetinic, I., & Mahadevan, A. (2015). Eddy-driven subduction exports particulate organic carbon from the spring bloom. *Science*, *348*(6231), 222–225. https://doi.org/10.1126/science.1260062

Qiu, B., Chen, S., Klein, P., Torres, H., Wang, J., Fu, L., & Menemenlis, D. (2020). Reconstructing upper-ocean vertical velocity field from sea surface height in the presence of unbalanced motion. *Journal of Physical Oceanography*, *50*(1), 55–79. https://doi.org/10.1175/JPO-D-19-0172.1

Qu, L. X., Thomas, L. N., Wienkers, A. F., Hetland, R. D., Kobashi, D., Taylor, J. R., et al. (2022). Rapid vertical exchange at fronts in the Northern Gulf of Mexico. *Nature Communications*, *13*(1), 5624. https://doi.org/10.1038/s41467-022-33251-7

Savelyev, I., Thomas, L. N., Smith, G. B., Wang, Q., Shearmann, R. K., Haack, T., et al. (2018). Aerial observations of symmetric instability at the north wall of the gulf stream. *Geophysical Research Letter*, *45*(1), 236–244. https://doi.org/10.1002/2017GL075735

Sea Level Anomaly. (2023). Global ocean gridded L4 sea surface heights and derived variables reprocessed 1993 ongoing [Dataset]. *E.U Copernicus Marine Service Information (CMEMS), Marine Data Store (MDS)*. https://doi.org/10.48670/moi-00148

Siegelman, L., Klein, P., Riviere, P., Thompson, A. F., Torres, H. S., Flexas, M., & Menemenlis, D. (2020). Enhanced upward heat transport at deep submesoscale ocean fronts. *Nature Geoscience*, *13*(1), 50–55. https://doi.org/10.1038/s41561-019-0489-1

Su, Z., Wang, J. B., Klein, P., Thompson, A. F., & Menemenlis, D. (2018). Ocean submesoscales as a key component of the global heat budget. *Nature Communications*, *9*(1), 775. https://doi.org/10.1038/s41467-018-02983-w

Tarry, D. R., Essink, S., Pascual, A., Ruiz, S., Poulain, P., Özgökmen, T., et al. (2021). Frontal convergence and vertical velocity measured by drifters in the Alboran Sea. *Journal of Geophysical Research: Oceans*, *126*(4), e2020JC016614. https://doi.org/10.1029/2020JC016614

Taylor, J. R., & Ferrari, R. (2009). On the equilibration of a symmetrically unstable front via a secondary shear instability. *Journal of Fluid Mechanics*, *622*, 103–113. https://doi.org/10.1017/S0022112008005272

Thomas, L. N. (2008). Formation of intrathermocline eddies at ocean fronts by wind-driven destruction of potential vorticity. *Dynamics of Atmospheres and Oceans*, *45*(3–4), 252–273. https://doi.org/10.1016/j.dynatmoce.2008.02.002

Thomas, L. N., & Lee, C. M. (2005). Intensification of ocean fronts by down-front winds. *Journal of Physical Oceanography*, *35*(6), 1086–1102. https://doi.org/10.1175/Jpo2737.1

Thomas, L. N., & Taylor, J. R. (2010). Reduction of the usable wind-work on the general circulation by forced symmetric instability. *Geophysical Research Letter*, *37*(18), L18606. https://doi.org/10.1029/2010gl044680

Thomas, L. N., Taylor, J. R., Ferrari, R., & Joyce, T. M. (2013). Symmetric instability in the Gulf Stream. *Deep-Sea Research Part II*, *91*, 96–110. https://doi.org/10.1016/j.dsr2.2013.02.025

Thompson, A. F., Lazar, A., Buckingham, C., Naveira Garabato, A. C., Damerell, G. M., & Heywood, K. J. (2016). Open-ocean submesoscale motions: A full seasonal cycle of mixed layer instabilities from gliders. *Journal of Physical Oceanography*, *46*(4), 1285–1307. https://doi.org/10.1175/jpo-d-15-0170.1

Wang, Q. Y., Dong, C. M., & Dong, J. H. (2024). Seasonality of Submesoscale vertical heat transport modulated by Oceanic mesoscale eddies in the Kuroshio extension. *Journal of Geophysical Research: Oceans*, *129*(10), e2024JC020939. https://doi.org/10.1029/2024JC020939

Whitt, D. B., Thomas, L. N., Klymak, J. M., Lee, C. M., & D'Asaro, E. A. (2018). Interaction of superinertial waves with submesoscale cyclonic filaments in the north wall of the gulf stream. *Journal of Physical Oceanography*, *48*(1), 81–99. https://doi.org/10.1175/Jpo-D-17-0079.1

Yang, H., & Chen, Z. (2023). Dataset for 2023GL106840 [Dataset]. *Zenodo*. https://doi.org/10.5281/zenodo.10428582

Yang, H. Y., Chen, Z., Sun, S., Li, M., Cai, W., Wu, L., et al. (2024). Observations reveal intense air-sea exchanges over submesoscale Ocean front. *Geophysical Research Letter*, *51*(2), e2023GL106840. https://doi.org/10.1029/2023GL106840

Yang, P. R., Jing, Z., Sun, B. R., Wu, L. X., Qiu, B., Chang, P., & Ramachandran, S. (2021). On the upper-ocean vertical eddy heat transport in the Kuroshio extension. Part I: Variability and dynamics. *Journal of Physical Oceanography*, *51*(1), 229–246. https://doi.org/10.1175/Jpo-D-20-0068.1

Yoshikawa, Y., Akitomo, K., & Awaji, T. (2001). Formation process of intermediate water in baroclinic current under cooling. *Journal of Geophysical Research*, *106*(C1), 1033–1051. https://doi.org/10.1029/2000jc000226

Yu, X., Naveira Garabato, A. C., Martin, A. P., Evans, D. G., & Su, Z. (2019). Wind-forced symmetric instability at a transient mid-ocean front. *Geophysical Research Letter*, *46*(20), 11281–11291. https://doi.org/10.1029/2019GL084309

Zhang, Z. (2024). Submesoscale dynamic processes in the South China Sea. *Ocean-Land-Atmosphere Research*, *3*, 45. https://doi.org/10.34133/olar.0045

Zheng, R., & Jing, Z. (2024). Diurnal variability of mixed layer overturning instabilities from glider array observations in the South China Sea. *Geophysical Research Letters*, *51*(11). https://doi.org/10.1029/2023gl107694

Zhou, H., Dewar, W., Yang, W., Liu, H., Chen, X., Li, R., et al. (2022). Observations and modeling of symmetric instability in the ocean interior in the Northwestern equatorial Pacific. *Communications Earth & Environment*, *3*(1), 28. https://doi.org/10.1038/s43247-022-00362-4

Zhu, R. C., Yang, H. Y., Li, M. K., Chen, Z. H., Ma, X., Cai, J. Z., & Wu, L. X. (2024). Observations reveal vertical transport induced by submesoscale front. *Scientific Reports*, *14*(1), 4407. https://doi.org/10.1038/s41598-024-54940-x